# PAPER

# Chemical speciation of heavy metals by surface-enhanced Raman scattering spectroscopy: identification and quantification of inorganic- and methyl-mercury in water†

Luca Guerrini,*[ab] Ignacio Rodriguez-Loureiro,[bc] Miguel A. Correa-Duarte,[c] Yih Hong Lee,[d] Xing Yi Ling,[d] F. Javier García de Abajo[ef] and Ramon A. Alvarez-Puebla*[abe]

Chemical speciation of heavy metals has become extremely important in environmental and analytical research because of the strong dependence that toxicity, environmental mobility, persistence and bioavailability of these pollutants have on their specific chemical forms. Novel nano-optical-based detection strategies, capable of overcoming the intrinsic limitations of well-established analytic methods for the quantification of total metal ion content, have been reported, but the speciation of different chemical forms has not yet been achieved. Here, we report the first example of a SERS-based sensor for chemical speciation of toxic metal ions in water at trace levels. Specifically, the inorganic $Hg^{2+}$ and the more toxicologically relevant methylmercury ($CH_3Hg^+$) are selected as analytical targets. The sensing platform consists of a self-assembled monolayer of 4-mercaptopyridine (MPY) on highly SERS-active and robust hybrid plasmonic materials formed by a dense layer of interacting gold nanoparticles anchored onto polystyrene microbeads. The co-ordination of $Hg^{2+}$ and $CH_3Hg^+$ to the nitrogen atom of the MPY ring yields characteristic changes in the vibrational SERS spectra of the organic chemoreceptor that can be qualitatively and quantitatively correlated to the presence of the two different mercury forms.

## Introduction

Heavy metal ions are among the main pollutants of natural waters, representing a major concern to human health and the environment. Noteworthy, the toxicity of a specific metal ion does not only depend on its concentration level but is largely related to its chemical form. In fact, the speciation of a metal exercises a direct control over the environmental mobility, persistence and bioavailability.[1,2] Consequently, monitoring the distribution of the different chemical species, rather than the total metal content, is vital for a complete understanding of their complex chemistry and their environmental and health effects. Highly sensitive analytical methods for metal cation detection and quantification commonly rely on atomic absorption or emission spectroscopy,[3] cold vapor atomic fluorescence spectrometry (CVAFS) and inductively coupled plasma-mass spectrometry (ICP-MS).[4] In addition, speciation analysis requires pre-separation procedures that are usually based on chromatographic methods or on different approaches that profit from the diverse chemical/physical properties of the metal species.[4] However, these traditional high-performance techniques are generally expensive, time-consuming and incompatible with routine *in situ* measurements. In this regard, there has been a growing interest in developing alternative detection strategies capable of overcoming the intrinsic limitations of these well-established analytical methods. The need for the development of fast, simple on-site monitoring techniques is even more acute in speciation analysis, as the sample collection, pre-treatments and storage are the most critical steps determining the sensitive and accurate quantification of often labile species. A paradigmatic case study is mercury and

*[a]Departamento de Química Física e Inorgánica, Universitat Rovira i Virgili, Avda. Països Catalans 26, 43007 Tarragona, Spain. E-mail: luca.guerrini@ctqc.org; ramon.alvarez@urv.cat*

*[b]CTQC – Centro de Tecnologia Quimica de Cataluña, Carrer de Marcel·lí Domingo s/n, 43007 Tarragona, Spain*

*[c]Departamento de Química Física, Universidade de Vigo, and Centro de Investigación Biomédica (CINBIO), 36310, Vigo, Spain*

*[d]Division of Chemistry and Biological Chemistry, School of Physical and Mathematical Sciences, Nanyang Technological University, 637371, Singapore*

*[e]ICREA, Passeig Lluís Companys 23, 08010 Barcelona, Spain*

*[f]ICFO – Institut de Ciencies Fotoniques, Mediterranean Technology Park, 08860 Castelldefels (Barcelona), Spain*

its compounds, which are listed among the most dangerous elements for human and ecosystem health.[5,6] In particular, methylmercury, produced in natural environments by anaerobic bacteria,[7] is the most potent mercuric toxin, the impact of which is severely worsened by its tendency to undergo extremely high bioaccumulation through the aquatic food web.[4] The high volatility of methylmercury and the dynamic interconversion processes between different species represent major obstacles in the exact determination of mercury species in natural aqueous environments.[4] Sensors based on electrochemical techniques,[8] and optical methods employing colorimetric,[9–12] fluorometric,[11,13] and surface-enhanced Raman scattering[14–20] outputs, are rapidly evolving into highly sensitive and robust devices capable of finally matching the stringent requirements for their translation to reliable applications in on-site real-life mercury analysis. However, one of the main challenges that still needs to be successfully tackled is the inability of these novel techniques to discriminate between different mercury species.[1,21] In particular, all these reported strategies uniquely deal with the detection of the inorganic $Hg^{2+}$ form while the identification and quantification of the much more toxicologically relevant methylmercury is completely disregarded.

Surface-enhanced Raman scattering (SERS) spectroscopy is a vibrational spectroscopy that combines the intrinsically rich structural specificity and flexibility of Raman spectroscopy with the extremely high sensitivity provided by the dramatic intensification of the inelastic scattering from molecules located near/at nanostructured metal surfaces, where collective oscillations of conduction electrons of the plasmonic substrate are excited by interaction with light.[22,23] As a result, SERS has arisen as a powerful analytical tool that has been implemented during the last decade in a myriad of different applications, particularly in the fields of environmental analysis and monitoring,[24] biodetection, diagnostics and bioimaging.[25–27] SERS has also been applied to the identification of vibrationless species, such as monoatomic metal ions, either *via* indirect methods that correlate changes in the absolute SERS intensity of a Raman label in the presence of the analyte[14–17,28] or by direct detection when the atomic ions coordinate an organic chemoreceptor whose SERS spectrum contains characteristic spectral "fingerprints" that selectively informs about the type and extension of ion complexation.[19,29,30] The latter sensing approach offers several advantages[31] such as multiplexing capabilities.[19,29]

Herein, we demonstrate the first example of the potential use of SERS for the chemical speciation of heavy metal pollutants, specifically the identification and quantification at trace levels of $Hg^{2+}$ and $CH_3Hg^+$ toxins in aqueous solution. The sensing strategy profits from the unique and characteristic spectral changes produced by the complexation of the inorganic and organic mercury forms with an organic ligand, allowing us to selectively identify and quantify at trace levels the presence of the two different species. As a metal ion receptor, we select 4-mercaptopyridine (MPY), which is known to strongly bind gold surfaces *via* its mercapto group and coordinate both mercuric species *via* the nitrogen of the pyridine moiety in water.[32–35] MPY is self-assembled onto closely spaced gold nanoparticles anchored on polystyrene microparticles, forming a hybrid plasmonic composite structure that acts as a robust and highly SERS-active platform supporting a dense collection of hot spots.[30,36]

## Results and discussion

The fabrication of the Au NPs-decorated polystyrene beads (PS@Au) was performed as previously described.[30,37] Initially, PS beads of 3 μm diameter were consecutively coated with layers of polyelectrolytes of opposite charge *via* a layer-by-layer assembly protocol. Specifically, negatively charged polystyrenesulfonate (PSS) and positively charged branched-polyethylenimine (PEI) were deposited in an alternate fashion to yield a final external PEI shell with a compact collection of positive charges. Subsequently, a large excess of negatively charged citrate-coated gold nanoparticles of ~55 nm diameter were left to adhere by electrostatic interaction onto the so-functionalized PS beads, generating hybrid plasmonic micro-particles with a dense homogenous coating of interacting nanostructures. Finally, extensive washing cycles were performed to ensure the removal of unbound nanoparticles. Fig. 1A and B shows representative ESEM and TEM images of PS beads coated with Au nanoparticles (PS@Au), whereas Fig. 1C and D illustrates the high resolution plasmonic characterization of an isolated PS@Au bead dried over a $SiO_x$/Si substrate performed *via* cathodoluminescence (CL) hyperspectral imaging. Two maxima can be identified in the CL spectrum: a strong plasmon contribution at ~538 nm, attributed to the longitudinal coupling of surface plasmon resonances between nanoparticles and a weaker blue-shifted shoulder at ~504 nm, which we ascribe to dipolar plasmon modes of interacting nanoparticles and/or LSPR of isolated nanoparticles, both in vacuum.

These easily-fabricated composite materials behave as robust microscopic carriers of large ensembles of closely spaced nanoparticles, concentrating a high number of interparticle hot-spots in a dense external shell whose averaged plasmonic response ensures very good homogeneity from bead to bead
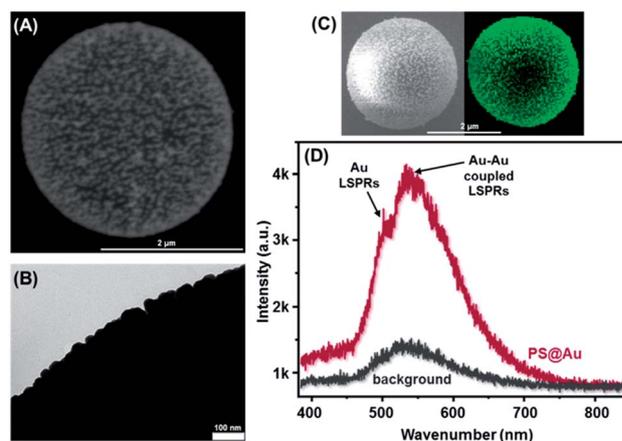


**Fig. 1** Representative ESEM (A) and TEM (B) images of PS@Au beads. (C) SEM image and photon map centered at 550 nm of a single PS@Au bead and (D) its corresponding CL spectrum.

SERS enhancing properties, as well as long-term optical stability.[36,38] As a result, intense and reproducible SERS signals can be obtained with very low bead concentration in suspension, making such hybrid SERS substrates particularly suitable for sensing applications.[30,37] Additionally, their resistance against aggregation offers a remarkable experimental flexibility regarding their manipulation and storage, which largely lacks in their colloidal counterparts (for instance, centrifugation/ redispersion steps can be performed at will without affecting the stability of the substrate, as well as changes in solvent, ionic strength *etc.*).

4-Mercaptopyridine (MPY) is a bifunctional molecule which is well-known to chemisorb onto Au surfaces *via* a metal–sulfur bond, generating an ordered, densely packed monolayer where MPY molecules are preferentially oriented perpendicularly with respect to the metal surface, thus exposing the pyridinic nitrogen to the bulk solution.[39,40] The corresponding SERS spectra of MPY have been thoroughly investigated and detailed vibrational band assignments can be found in the literature (the main band assignments and wavenumber positions are listed in Table S1†).[39,41–44] Fig. 2 (green line) illustrates the characteristic MPY SERS spectrum at neutral pH.[42] It has been shown that the coordination of metal ions to the pyridinic nitrogen atom leads to a redistribution of the electrons among different bonds within the aromatic ring, and such perturbation is directly reflected in the vibrational spectrum of the molecule.[45–47] This can be clearly observed in the MPY spectrum upon complexation with $Hg^{2+}$ (Fig. 2, blue curve), where remarkable alteration of the ligand spectral profile is revealed, in terms of both



**Fig. 2** SERS spectra of 4-mercaptopyridine (MPY) on PS@Au beads before and after the exposure to $HgCl_2$ 20 ppb and $CH_3HgCl$ 15.1 ppb solutions (final concentration of beads in the analyte solution = 0.8 µg mL⁻¹). SERS spectra are normalized to the ring breathing band at 1096 cm⁻¹. The dotted-curves are the difference spectra obtained by subtracting the SERS of free MPY from the corresponding spectra in the presence of $HgCl_2$ 20 ppb and $CH_3HgCl$ 15.1 ppb. The Raman background of the plastic container (Fig. S7†) was subtracted from each spectrum (residual weak narrow bands at *ca.* 808 and 841 cm⁻¹, ascribed to the plastic, may still appear in some spectra).

frequency shifts and relative intensities as further highlighted by digital subtraction of the SERS signal of the free ligand from the spectrum of the MPY–$Hg^{2+}$ surface complex (Fig. 2, blue dotted curve). Several spectral features are worth commenting on. First of all, we observe a general mild increase in the frequency of the in-plane $a_1$ pyridine modes such as those at 702 cm⁻¹, ascribed to $\beta(CC)/\nu(CS)$ modes, at 1001 cm⁻¹, originating in pure ring breathing vibration, at 1040 cm⁻¹, attributed to a $\beta(CH)$ mode, at 1096 cm⁻¹, resulting from the mixed contributions of ring breathing and $\nu(CS)$ modes, and at 1612 cm⁻¹, assigned to $\nu(C{=}C)/\nu(C{=}N)$ vibrations. Second, we highlight a notable intensity increase of the mixed ring breathing/$\nu(CS)$ band at 1096 cm⁻¹, and the band at 1580 cm⁻¹, assigned to $\nu(C{=}C)/\nu(C{=}N)$ vibrations that are characteristic of the N-deprotonated form, especially with respect to the features at 1001, 1040, 1276 and 1612 cm⁻¹. Overall, such changes are consistent with the complexation of metal ions with the N atom of MPY.[45–47] Additionally, since attractive π–π interactions between MPY molecules adsorbed on Au surfaces take place for high surface coverage,[40] we cannot rule out a cascade amplification where coordination of a metal ion on one pyridinic ring is indirectly "felt" by other proximal MPY molecules. It is worthy to note that the largest relative intensity decrease is recorded for the out-of-plane C–H deformation band at 777 cm⁻¹. As we can reasonably expect that changes in the electron density of the aromatic ring only produce a poor perturbation of the modes involving hydrogen motions, this spectral change suggests a reorientation of the $Hg^{2+}$-coordinated-MPY molecules toward a more perpendicular position onto the metal surface, in agreement with the surface selection rules.[48,49] Structural studies of pyridine (py) coordinated to $Hg^{2+}$ in aqueous solution showed that $Hg(py)_n$ complexes predominantly exist for $n = 2$ (and, to a lesser extent, for 3 and 4 pyridine unity),[46] and the metal coordination mostly occurs *via* σ-electron donation from the N to $Hg^{2+}$ with negligible π-back bonding from the metal ion.[32–34] Thus, we can argue that the chelation of $Hg^{2+}$ *via* multidentate N-bonding is also favored with MPY molecules in the densely packed self-assembled monolayer that exists onto the gold surface.

In contrast, methylmercury ($CH_3Hg^+$) has a strong tendency toward a linear two-coordinate geometry,[34,50,51] and therefore establishes unidentate complexes with pyridine in solution with formation constants only slightly smaller than $Hg(py)_n$ [$pK_a = 4.8$ for mono pyridine coordination with $CH_3Hg^+$ (ref. 35) whereas the first two pyridine constants in $Hg(py)_2$ are almost equal: 5.1 and 4.9, respectively[52]]. However, competing reactions in aqueous media generally reduce the extent to which $CH_3Hg^+$ complexes organic ligands.[35] Fig. 2 (red line) shows the SERS spectra of the MPY ligand in the presence of $CH_3Hg^+$. Strikingly, two new intense bands arise at 526 and 1167 cm⁻¹, which are assigned to the stretching and bending modes, respectively, of the Hg–$CH_3$ group binding the MPY ligand.[50,53] Importantly, when $CH_3Hg^+$ is directly adsorbed onto the unfunctionalized gold surface (Fig. S4†), the corresponding vibrational modes appear at very different wavenumbers, providing clear evidence of both the effective formation of the MPY–$HgCH_3$ complex and the existence of a densely packed self-assembled monolayer of
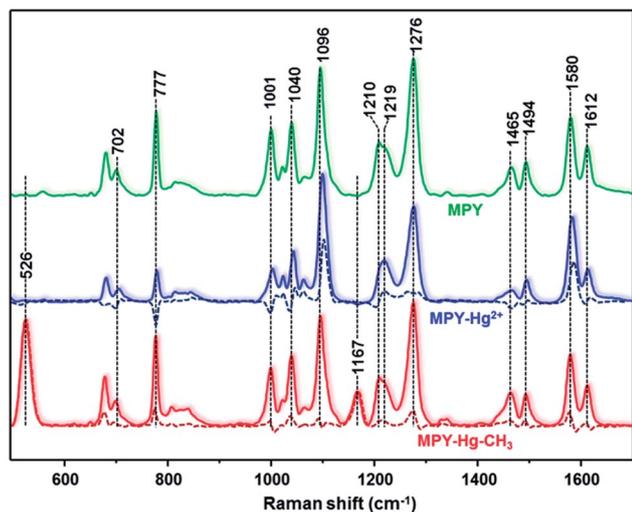
the molecular receptor on the metal nanoparticles that hampers the diffusion of the analyte to the gold surface. This conclusion is further supported by the lack of significant changes in the overall SERS intensity upon the addition of both mercury species (*i.e.* none/few MPY molecules were displaced from the metal surface by the analytes, see Fig. S5A†). Additionally, thiophenol (TP) was selected as a control molecule to investigate the potential intercalation of the mercury species in the –S–Au bond. No changes in the SERS profile of TP were revealed even in the presence of high $Hg^{2+}$ and $CH_3Hg^+$ concentrations (*i.e.*, no intercalation occurs, see Fig. S5B†), providing further evidence that mercury–MPY interaction takes place *via* the aromatic nitrogen atom.

Unlike what was observed for $Hg^{2+}$, the SERS features of MPY are much less affected by the metal complexation with $CH_3Hg^+$ (Fig. 2, red dotted-line, difference spectrum obtained by removing the SERS signal of the free ligand from the spectrum of the MPY–$HgCH_3$ surface complex). This discrepancy from what we previously observed for $Hg^{2+}$ coordination can be ascribed to the much weaker acidic properties of $CH_3Hg^+$, which is expected to produce a corresponding lower alteration of the electron density in the aromatic ring. Additionally, it is reasonable to speculate that the unidentate interaction of $CH_3Hg^+$ can perturb the orientation of the coordinated MPY molecules much less than the adoption of a multidentate geometry around the $Hg^{2+}$ ion.

The SERS response of the sensing device was also tested against several other ions, such as $Mg^{2+}$, $Pb^{2+}$, $Ni^{2+}$, $Co^{2+}$, $Cd^{2+}$ and $Zn^{2+}$. The SERS spectrum of the ligand was left completely or largely unaltered upon the addition of such metals at high concentration ($10^{-6}$ M, Fig. S6†), thus indicating that MPY has excellent SERS selectivity for $Hg^{2+}$ and $CH_3Hg^+$-sensing.

The differences in the spectral profiles of MPY coordinated either with inorganic or methylmercury are so remarkable that an effective SERS speciation can be easily achieved even without the need for any advanced multivariate data analysis. In fact, metal ion concentrations were quantitatively correlated with the spectral changes using the following ratiometric peak intensities: (a) $I_{777}/I_{1096}$ for $Hg^{2+}$ [ratio between the C–H deformation at 777 $cm^{-1}$ and the mixed ring breathing/$\nu$(CS) band at 1096 $cm^{-1}$, which showed the highest ±variation rate in the presence of the analyte] and (b) $I_{526}/I_{1096}$ for $CH_3Hg^+$ (ratio between the most intense Hg–$CH_3$ vibrational feature in the spectrum and the ring breathing band at 1096 $cm^{-1}$).

Fig. 3 illustrates four representative SERS spectra obtained in the presence of increasing $Hg^{2+}$ amounts together with an inset figure describing the metal-ion concentration dependence of the $I_{777}/I_{1096}$ ratio. SERS spectra were normalized to the band at 1096 $cm^{-1}$, whereas the band at 777 $cm^{-1}$ was highlighted in blue to show its gradual weakening with increasing $Hg^{2+}$ concentration. In the inset figure, three calibration lines are plotted, corresponding to data sets obtained at different PS@Au bead dilutions. The dynamic range for metal ion detection by SERS was indeed controlled by adjusting the beads concentration because for our sensing purpose, a densely packed SAM of the molecular receptor is required on the metal surface (*i.e.*, the density of MPY binding sites on the gold surface remains
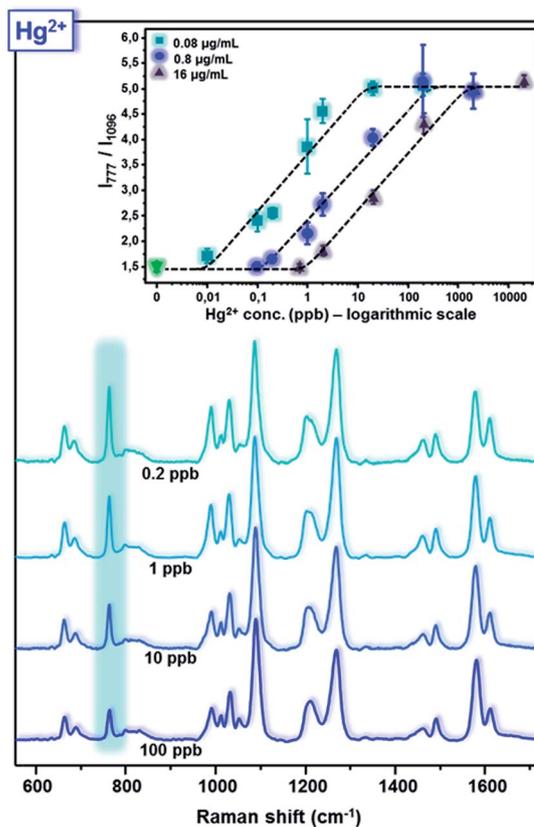


Fig. 3 SERS spectra of MPY on PS@Au beads upon exposure to $HgCl_2$ solutions of different concentration (final concentration of beads in solution = 0.8 µg $mL^{-1}$). SERS spectra are normalized to the ring breathing band at 1096 $cm^{-1}$. Inset: intensity ratio, $I_{1096}/I_{799}$, of the MPY analyte-sensitive bands at 1096 and 799 $cm^{-1}$ as a function of $Hg^{2+}$ concentration (logarithmic scale) for different bead concentrations in the metal ion solutions: (a) 16 µg $mL^{-1}$, (b) 0.8 µg $mL^{-1}$ and (c) 0.08 µg $mL^{-1}$. The corresponding detection limits are 2 ppb, 0.1 ppb and 50 ppt, respectively. Error bars are equal to two standard deviations ($N = 3$).

unchanged). The SERS spectra were then recorded by fixing the amount of PS@Au–MPY beads (10 µL of a 0.4 mg $mL^{-1}$ suspension) and exposing it to progressively larger volumes of $Hg^{2+}$ aqueous solutions (500 µL, 10 mL and 50 mL, corresponding to 16, 0.8 and 0.08 µg $mL^{-1}$ final bead concentration, respectively). The mixtures were left under gentle shaking for 2 hours before being centrifuged to 50 µL final volume, thoroughly sonicated and finally investigated by SERS in suspension. Pre-concentration of the beads to such a small volume allows obtaining very intense SERS signals for short exposure time (10 s, 1 accumulation) with high spectral reproducibility since the acquired SERS spectra are ensemble-average measurements of a large number of PS@Au–MPY units. As can be seen from the inset in Fig. 3, all plots of $I_{777}/I_{1096}$ *vs.* $Hg^{2+}$ concentration (ppb) reveal linear correlations for an interval of approximately 3 orders of magnitude (logarithmic scale), with progressively lower detection limits as the bead dilution is increased (2 ppb, 0.1 ppb and 50 ppt, respectively) and high-quality squared correlation coefficient values ($r^2 = 0.98$, 0.99 and 0.94, respectively). Importantly, the sensitivity of the sensor

response (*i.e.* the slope of the regression line) remains constant regardless of the bead dilution. Thus, a detection limit of several orders of magnitude lower than the U.S.A was observed. EPA-defined maximum level in drinking water[54] has been easily achieved by trivial sample dilution thanks to the high SERS activity and optical stability of the PS@Au beads. We foresee, for instance, that the simple incorporation of PS@Au beads in common microfluidic channels for analyte accumulation would further increase the sensitivity of this method.

In qualitative agreement with the observations of Fig. 2, the quantitative spectral response of MPY upon exposure to $CH_3Hg^+$ solution at increasing concentrations diverges from the $Hg^{2+}$ behavior. SERS spectra and plot (A) in Fig. 4 indicate a linear increase of the $I_{526}/I_{1096}$ ratio in the ~0–15 ppb range of analyte concentration for a final bead concentration of 0.8 μg $mL^{-1}$ (linear scale; $r^2 > 0.98$; limit of detection 1.5 ppb). Once again, the SERS spectra were normalized to the band at

1096 $cm^{-1}$, whereas the $\nu(Hg–CH_3)$ band at 526 $cm^{-1}$ was highlighted in yellow. The high limit of detection achieved for $CH_3Hg^+$ as compared to $Hg^{2+}$ under the same experimental conditions (1.5 ppb *vs.* 0.1 ppb, respectively, for the final concentration of beads in solution = 0.8 μg $mL^{-1}$) is consistent with the lower affinity of this soft Lewis acid for pyridinic ligands. Interestingly, in this case a saturation plateau of the $I_{526}/I_{1096}$ ratio is not reached for higher $CH_3Hg^+$ concentration but, on the contrary, a notable drop in the relative intensity of the $\nu(Hg–CH_3)$ band is observed. As a representative example, the SERS spectrum obtained in the presence of $CH_3Hg^+$ 216 ppb is illustrated in Fig. 4, pink curve. Here we observe, as for $Hg^{2+}$, a marked relative intensity increase of the ring breathing/$\nu(CS)$ band at 1096 and the "N-deprotonated" feature at 1580 $cm^{-1}$, especially compared to the pure ring breathing contribution at 1001 $cm^{-1}$ and that of the "N-protonated" band at 1612 $cm^{-1}$. Such features also undergo a slight red-shift of their peak position. However, different to what occurred for $Hg^{2+}$, the out-of-plane C–H deformation band at 777 $cm^{-1}$ and the in-plane C–H bending at 1040 $cm^{-1}$ do not suffer from relevant alterations of both their relative intensity and peak position. This peculiar change in spectral the pattern is independent of the $CH_3Hg^+$ concentration in the bulk solution and occurs at approximately the same [analyte]/[beads] ratio (Fig. S8 and S9†), indicating that the transition from these two different coordination regimes is mainly related to the analyte surface crowding. These findings seem to suggest a chemical transformation of the pyridine-coordinated $CH_3Hg^+$ species when a threshold surface density is achieved. Nonetheless, as highlighted in Fig. 4, plot B, the $I_{777}/I_{1096}$ ratio in the detection of $CH_3Hg^+$ shows minimal variation around the free ligand sample value even for high analyte concentration, thus preserving the spectral differentiation between the two mercury species.

Interestingly, SERS analysis of premixed inorganic/organic mercury solutions at ppb levels reveal spectral changes in the
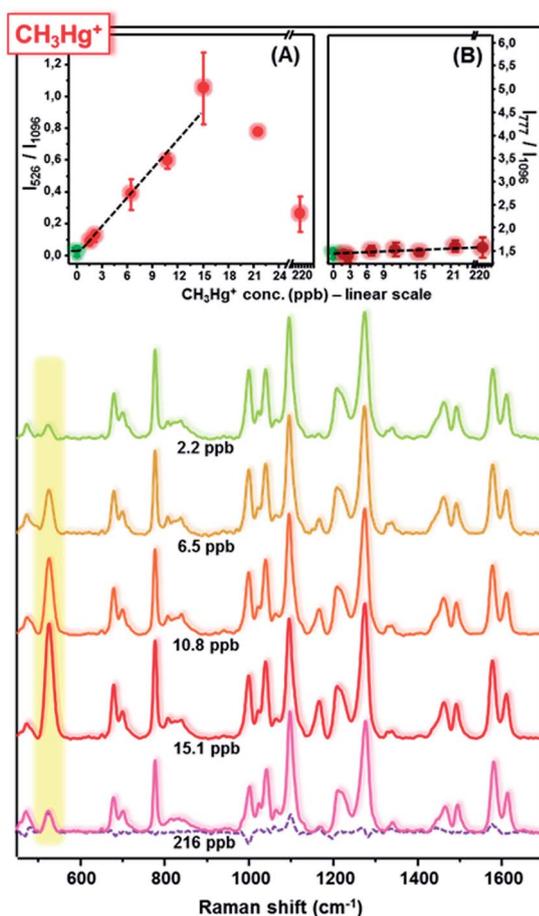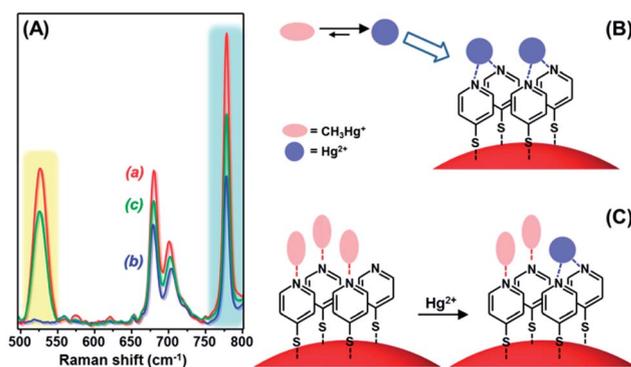


Fig. 4 SERS spectra of MPY on PS@Au beads upon the exposure to $CH_3Hg^+$ solutions of different concentrations (final concentration of beads in solution = 0.8 μg $mL^{-1}$). SERS spectra are normalized to the ring breathing band at 1096 $cm^{-1}$. Insets: (A) intensity ratio, $I_{526}/I_{1096}$, of the $\nu(Hg–CH_3)$ band at 526 $cm^{-1}$ and the MPY ring breathing band at 1096 $cm^{-1}$ (detection limit 1.5 ppb) and (B) intensity ratio, $I_{1096}/I_{799}$, of the MPY bands at 1096 and 799 $cm^{-1}$, as a function of $CH_3Hg^+$ concentration (linear scale; bead concentration in the metal solutions equals to 0.8 μg $mL^{-1}$). Error bars are equal to two standard deviations ($N = 3$).



Fig. 5 (A) SERS spectra in the 500–800 $cm^{-1}$ range of MPY on PS@Au beads upon the addition of (a) $CH_3Hg^+$ (12 ppb, final concentration) and (b) a mixture of $Hg^{2+}$ and $CH_3Hg^+$ (3 ppb and 12 ppb, respectively, final concentration). (c) SERS spectrum acquired upon the addition of $Hg^{2+}$ (3 ppb, final concentration) to the sample (a). Final concentration of beads in solution = 0.8 μg $mL^{-1}$. SERS spectra are normalized to the ring breathing band at 1096 $cm^{-1}$. (B and C) Schematic outlines of the coordination processes corresponding to the spectra (b) and (c), respectively.

MPY vibrational profile that are solely ascribed to the coordination of $Hg^{2+}$ (Fig. 5A, blue curve, for $Hg^{2+}$ and $CH_3Hg^+$, 3 ppb and 12 ppb, respectively). In contrast, when the addition of $Hg^{2+}$ is performed in a second step after the coordination of $CH_3Hg^+$ to MPY, the characteristic methylmercury features, such as the intense band at 526 $cm^{-1}$ (Fig. 5A, red curve) are retained in the SERS spectrum of the mixture (Fig. 5A, green curve). These results suggest that under the investigated experimental conditions, an extended decomposition of the methylmercury form is triggered in solution by the presence of the inorganic $Hg^{2+}$, unless $CH_3Hg^+$ species are previously stabilized by coordination to MPY ligand (Fig. 5B and C tentatively outline the two different processes). These findings are consistent with the dynamic interconversion of the two species in water, specifically with the shift of the equilibrium from the chemically labile $CH_3Hg^+$ to the more stable $Hg^{2+}$ form.[55]

## Experimental

### Materials

All chemicals were purchased from Sigma-Aldrich and used as received. Milli-Q water was used throughout the experiments.

### Synthesis of Au colloids

Small gold nanoparticles (Au seeds) of ~15 nm diameter were prepared according to the Turkevich–Frens preparation method.[56,57] Briefly, $HAuCl_4$ trihydrate (15 mg) was dissolved in Milli-Q water (150 mL) and heated to boiling. An aqueous solution of trisodium citrate (1% w/w, 4.5 mL) was then quickly added under vigorous stirring, and the mixture was refluxed for 30 more minutes. The solution was then allowed to cool to room temperature under gentle stirring for several hours. Large gold nanoparticles of ~55 ± 3 nm (Fig. S1†) were prepared by following the previously reported seeded growth method.[28] Briefly, 125 mL of a solution of $HAuCl_4$ trihydrate (14.57 mg) in Milli-Q water were heated to boiling; then, under vigorous stirring, 3.75 mL of Au seeds and 2.56 mL of an aqueous solution of trisodium citrate (1% w/w) were consecutively added to the solution. The mixture was refluxed for 30 minutes before adding 4.3 mL of a 4.6% w/w trisodium citrate aqueous solution. The solution was finally allowed to boil for another hour and let to cool down to room temperature under gentle stirring for several hours.

### Assembly of PS@Au microbeads

Polystyrene microbeads of 3 μm diameter (0.5 mL of a 100 mg $mL^{-1}$ suspension) were first wrapped with alternating polyelectrolyte monolayers using the layer-by-layer (LbL) electrostatic self-assembly protocol.[37,58] Alternate layers of negatively charged polystyrenesulfonate (PSS, $M_w$ = 1 000 000) and positively charged branched-polyethylenimine (PEI, $M_w$ = 25 000) were deposited in the following order: PSS, PEI, PSS and PEI. Specifically, polystyrene microbeads (0.5 mL of a 100 mg $mL^{-1}$ suspension) were added to 25 mL of a 2 mg $mL^{-1}$ PSS aqueous solution containing 0.5 M NaCl. After 30 min of sonication and 2 hours of agitation, the PS microbeads were extensively washed

with Milli-Q water and centrifuged (5800 rpm, 20 min). An identical protocol (concentrations, elapsed times, and washing protocol) was applied for depositing subsequent layers of polyelectrolytes. Finally, the PS beads were redispersed in 10 mL of Milli-Q water (final concentration = 5 mg $mL^{-1}$).

The adsorption of the particles onto the polyelectrolytes-wrapped PS beads (5 mg $mL^{-1}$) was carried out by adding a large excess of Au colloids in order to achieve the highest possible surface coverage density onto the PS beads. Specifically, 10 mL of PS beads (5 mg $mL^{-1}$) were added to 50 mL of gold colloids (55 nm diameter nanoparticles). After 30 min of sonication, the PS@Au beads were left under shaking condition for 2 hours and then left at rest overnight for decantation. The clear supernatant was removed and the whole process was repeated four more times until the supernatant retained a reddish color, characteristic of gold colloids in suspension. Then, the mixture was washed first for three times by centrifugation (2000 rpm, 25 min) and subsequently, three times more by decantation with Milli-Q water to remove any unbound Au NPs from the mixture. The samples were finally redispersed to 10 mL in Milli-Q (5 mg $mL^{-1}$ final concentration of PS@Au beads). Representative TEM and ESEM images of PS@Au particles are also reported in Fig. S2,† whereas the optical extinction spectra of PS@Au and PS suspensions, as well as Au NP colloids, are illustrated in Fig. S3.†

### Functionalization of PS@Au beads with 4-mercaptopyridine (MPY)

0.4 mL of PS@Au beads (5 mg $mL^{-1}$) were added to 5 mL of an ethanolic solution of 4-mercaptopyridine, MPY, $10^{-2}$ M, and left under agitation for 48 hours (the sample was also repeatedly sonicated during this aging step to guarantee the optimal dispersion of the beads) in order to obtain a well-packed SAM of the ligand onto the metal surface. Extensive washing of the PS@Au–MPY beads was performed to eliminate unbound MPY molecules from the solution, which consisted 5 centrifugation/washing steps with 10 mL of ethanol and 2 centrifugation/washing steps with 10 mL of Milli-Q water. Finally, PS@Au–MPY beads were redispersed in 5 mL of Milli-Q water (0.4 mg $mL^{-1}$). PS@Au beads functionalized with thiophenol (TP) as an experimental control were prepared following the same procedure.

### SERS detection of $Hg^{2+}$ and $CH_3Hg^+$ with PS@Au–MPY beads

10 μL of a sonicated PS@Au–MPY suspension were added to a fresh aqueous solution of $HgCl_2$ or $CH_3HgCl$ of variable concentration (pH ~ 7) and left under shaking for 2 hours before being centrifuged to 50 μL (final volume) and immediately investigated by SERS. Progressively lower detection limits were obtained by increasing the analyte volume solutions from 0.5 mL to 10 mL and, finally, to 50 mL. The corresponding bead concentrations in the metal solutions were 16 μg $mL^{-1}$, 0.8 μg $mL^{-1}$ and 0.08 μg $mL^{-1}$, respectively. SERS measurements were obtained using 785 nm excitation and a long working distance objective (100% laser power, 1 accumulation, 10 s exposure time). The Raman background of the plastic container (Fig. S7†) was subtracted from each spectrum,

although some residual weak narrow bands ascribed to the plastic still appeared in some spectra.

### Instrumentation

SERS experiments were conducted using a Renishaw InVia Reflex confocal microscope equipped with a high-resolution grating consisting of 1200 grooves per cm for NIR wavelengths, additional band-pass filter optics, and a CCD camera. UV-vis spectra were recorded using a Thermo Scientific Evolution 201 UV-visible spectrophotometer. Transmission electron microscopy (TEM) was performed with a JEOL JEM-1011 transmission electron microscope. Environmental scanning electron microscopy (ESEM) was performed with a JEOL 6400 scanning electron microscope. Quantitative cathodoluminescence was carried out using an Attolight Rosa 4634 microscope, which tightly integrates a high-speed achromatic reflective lens (N.A. 0.72) within the objective lens of a field emission gun scanning electron microscope (FEG-SEM). Cathodoluminescence was spectrally resolved with a Czerny–Turner spectrometer (Horriba-JY iHR320, 320 mm focal length, 150 grooves per mm grating) and measured with an Andor Newton EM-CCD (EM-970P-BV). Electron beam energies of 8 kV were used to excite the samples. The beam dwell time was set to 0.2 s.

## Conclusions

In summary, we report the first example of a SERS-based sensor for chemical speciation of $Hg^{2+}$ and $CH_3Hg^+$. 4-Mercaptopyridine was selected as an organic chemoreceptor capable of (i) strongly binding to gold nanoparticles organized on polystyrene microbeads in highly SERS active hybrid materials and (ii) coordinating both mercury species via its aromatic nitrogen, yielding corresponding $MPY–Hg^{2+}$ and $MPY–(Hg–CH_3)^+$ surface complexes with different SERS spectra. The characteristic spectral changes in the chemoreceptor SERS profile upon metal coordination enabled the effective chemical speciation between the inorganic and organic-mercury forms and were also quantitatively correlated with the metal ion concentrations for their detection at trace levels.

## Acknowledgements

## References

1  K. Leopold, M. Foulkes and P. Worsfold, Anal. Chim. Acta, 2010, **663**, 127–138.

2  M. Kelly, W. J. Allison, A. R. Garman and C. J. Symon, Mining and the Freshwater Environment, Elsevier, Essex, England, 1988.

3  K. W. Jackson and T. M. Mahmood, Anal. Chem., 1994, **66**, R252–R279.

4  Y. Gao, Z. M. Shi, Z. Long, P. Wu, C. B. Zheng and X. D. Hou, Microchem. J., 2012, **103**, 1–14.

5  ATSDR (Agency for Toxic Substances and Disease Registry), Priority List of Hazardous Substances, http://www.atsdr.cdc.gov/spl/.

6  European Commission, Priority substances under the Water Framework Directive, http://ec.europa.eu/environment/water/water-framework/priority_substances.htm.

7  A. J. Poulain and T. Barkay, Science, 2013, **339**, 1280–1281.

8  M. Leermakers, W. Baeyens, P. Quevauviller and M. Horvat, TrAC, Trends Anal. Chem., 2005, **24**, 383–393.

9  Z. Guo, Z.-G. Liu, X.-Z. Yao, K.-S. Zhang, X. Chen, J.-H. Liu and X.-J. Huang, Sci. Rep., 2013, **3**, 3115.

10  J. S. Lee, M. S. Han and C. A. Mirkin, Angew. Chem., Int. Ed., 2007, **46**, 4093–4096.

11  X. J. Xue, F. Wang and X. G. Liu, J. Am. Chem. Soc., 2008, **130**, 3244–3245.

12  H. N. Kim, W. X. Ren, J. S. Kim and J. Yoon, Chem. Soc. Rev., 2012, **41**, 3210–3244.

13  C. Diez-Gil, R. Martinez, I. Ratera, T. Hirsh, A. Espinosa, A. Tarraga, P. Molina, O. S. Wolfbeis and J. Veciana, Chem. Commun., 2011, **47**, 1842–1844.

14  Y. K. Yang, K. J. Yook and J. Tae, J. Am. Chem. Soc., 2005, **127**, 16760–16761.

15  L. Zhang, H. X. Chang, A. Hirata, H. K. Wu, Q. K. Xue and M. W. Chen, ACS Nano, 2013, **7**, 4595–4600.

16  W. Ren, C. Z. Zhu and E. K. Wang, Nanoscale, 2012, **4**, 5902–5909.

17  T. Senapati, D. Senapati, A. K. Singh, Z. Fan, R. Kanchanapally and P. C. Ray, Chem. Commun., 2011, **47**, 10326–10328.

18  D. Han, S. Y. Lim, B. J. Kim, L. Piao and T. D. Chung, Chem. Commun., 2010, **46**, 5587–5589.

19  E. Chung, R. Gao, J. Ko, N. Choi, D. W. Lim, E. K. Lee, S. I. Chang and J. Choo, Lab Chip, 2013, **13**, 260–266.

20  V. M. Zamarion, R. A. Timm, K. Araki and H. E. Toma, Inorg. Chem., 2008, **47**, 2934–2936.

21  S. Botasini, G. Heijo and E. Mendez, Anal. Chim. Acta, 2013, **800**, 1–11.

22  K. A. Willets and R. P. Van Duyne, Annu. Rev. Phys. Chem., 2007, **58**, 267–297.

23  M. Moskovits, Rev. Mod. Phys., 1985, **57**, 783–826.

24  R. A. Alvarez-Puebla and L. M. Liz-Marzan, Energy Environ. Sci., 2010, **3**, 1011–1017.

25  R. A. Alvarez-Puebla and L. M. Liz-Marzan, Small, 2010, **6**, 604–610.

26  S. Abalde-Cela, P. Aldeanueva-Potel, C. Mateo-Mateo, L. Rodriguez-Lorenzo, R. A. Alvarez-Puebla and L. M. Liz-Marzan, J. R. Soc., Interface, 2010, **7**, S435–S450.

27  K. Saha, S. S. Agasti, C. Kim, X. N. Li and V. M. Rotello, Chem. Rev., 2012, **112**, 2739–2779.

28  Z. Krpetic, L. Guerrini, I. A. Larmour, J. Reglinski, K. Faulds and D. Graham, Small, 2012, **8**, 707–714.

29  D. Tsoutsi, L. Guerrini, J. M. Hermida-Ramon, V. Giannini, L. M. Liz-Marzan, A. Wei and R. A. Alvarez-Puebla, Nanoscale, 2013, **5**, 5841–5846.

30 D. Tsoutsi, J. M. Montenegro, F. Dommershausen, U. Koert, L. M. Liz-Marzan, W. J. Parak and R. A. Alvarez-Puebla, *ACS Nano*, 2011, **5**, 7539–7546.

31 R. A. Alvarez-Puebla and L. M. Liz-Marzan, *Angew. Chem., Int. Ed.*, 2012, **51**, 11214–11223.

32 T. Ibusuki and Y. Saito, *Inorg. Chim. Acta*, 1976, **19**, 87–90.

33 A. J. Canty, C. L. Raston, B. W. Skelton and A. H. White, *J. Chem. Soc., Dalton Trans.*, 1982, 15–18.

34 D. J. Brown, *The Chemistry of Heterocyclic Compounds, Pyridine Metal Complexes*, Wiley-Interscience, 1985.

35 D. L. Rabenstein, *Acc. Chem. Res.*, 1978, **11**, 100–107.

36 M. Spuch-Calvar, L. Rodriguez-Lorenzo, M. P. Morales, R. A. Alvarez-Puebla and L. M. Liz-Marzan, *J. Phys. Chem. C*, 2009, **113**, 3373–3377.

37 R. Ahijado-Guzman, P. Gomez-Puertas, R. A. Alvarez-Puebla, G. Rivas and L. M. Liz-Marzan, *ACS Nano*, 2012, **6**, 7514–7520.

38 S. Abalde-Cela, J. M. Hermida-Ramon, P. Contreras-Carballada, L. De Cola, A. Guerrero-Martinez, R. A. Alvarez-Puebla and L. M. Liz-Marzan, *ChemPhysChem*, 2011, **12**, 1529–1535.

39 H. Z. Yu, N. Xia and Z. F. Liu, *Anal. Chem.*, 1999, **71**, 1354–1358.

40 J. Kucera and A. Gross, *Langmuir*, 2008, **24**, 13985–13992.

41 J. Hu, B. Zhao, W. Xu, B. Li and Y. Fan, *Spectrochim. Acta, Part A*, 2002, **58**, 2827–2834.

42 Y. W. Chao, Q. Zhou, Y. Li, Y. R. Yan, Y. Wu and J. W. Zheng, *J. Phys. Chem. C*, 2007, **111**, 16990–16995.

43 J. A. Baldwin, B. Vlckova, M. P. Andrews and I. S. Butler, *Langmuir*, 1997, **13**, 3744–3751.

44 H. Guo, L. Ding and Y. J. Mo, *J. Mol. Struct.*, 2011, **991**, 103–107.

45 S. Akyuz, A. B. Dempster and S. Suzuki, *J. Mol. Struct.*, 1973, **17**, 105–125.

46 A. G. Brolo, M. Odziemkowski and D. E. Irish, *J. Raman Spectrosc.*, 1998, **29**, 713–719.

47 G. Mizutani and S. Ushioda, *J. Chem. Phys.*, 1989, **91**, 598–602.

48 M. Moskovits, *J. Chem. Phys.*, 1982, **77**, 4408–4416.

49 M. Moskovits and J. S. Suh, *J. Phys. Chem.*, 1984, **88**, 5526–5530.

50 A. J. Canty and A. Marker, *Inorg. Chem.*, 1976, **15**, 425–430.

51 A. J. Canty and C. V. Lee, *Organometallics*, 1982, **1**, 1063–1066.

52 J. Bjerrum, *Acta Chem. Scand.*, 1972, **26**, 2734–2742.

53 S. Alex and R. Savoie, *Can. J. Chem.*, 1987, **65**, 491–496.

54 United States Environmental Protection Agency (EPA), *National Primary Drinking Water Regulations (2009)*, http://water.epa.gov/drink/contaminants/upload/mcl-2.pdf.

55 W. Stumm and J. J. Morgan, *Aquatic Chemistry: Chemical Equilibria and Rates in Natural Waters*, John Wiley & Sons, 1995.

56 J. Turkevich, P. C. Stevenson and J. Hillier, *Discuss. Faraday Soc.*, 1951, 55–75.

57 G. Frens, *Nature (London), Phys. Sci.*, 1973, **241**, 20–22.

58 G. Decher, *Science*, 1997, **277**, 1232–1237.